Digital Discovery

ROYAL SOCIETY OF CHEMISTRY

PAPER

View Article Online
View Journal | View Issue

Open Access Article. Published on 14 March 2025. Downloaded on 1/8/2026 1:14:21 AM.
This article is licensed under a Creative Commons Attribution-NonCommercial 3.0 Unported Licence.

Check for updates

Cite this: *Digital Discovery*, 2025, **4**, 1100

Ligand design for ^{227}Ac extraction by active learning and molecular topology†

Jeffrey A. Laub and Konstantinos D. Vogiatzis *

Targeted α-therapy (TAT) is a promising radiotherapeutic technique for the treatment of various cancers due to the high linear energy transfer and low penetration depth of α-particles. Unfortunately, one of the major hindrances in the use of TAT is the accessibility of acceptable α-emitting radioisotopes. Of the acceptable radioisotopes, ^{223}Ra, ^{224}Ra, ^{225}Ra, and ^{225}Ac can all originate from ^{227}Ac. Being able to selectively isolate ^{227}Ac is crucial for aiding in increasing the accessibility of α-emitting radioisotopes for TAT. Some of the more successful ligands used for the selective separation of trivalent actinides are the 6,6′-bis(1,2,4-triazin-3-yl)-2,2′-bipyridine (BTBP)-based ligand family. Current ligand performance screening is accomplished by using a trial-and-error-based method which is expensive and based primarily on chemical intuition and previous studies. In this study, effective computer-aided ligand screening has been accomplished by generating $CyMe_4$–BTBP-based ligands and predicting stability constants for ^{227}Ac extraction of each using scalar relativistic density functional theory (DFT) followed by supervised machine learning (ML). DFT was used to compute stability constants from a 2 : 1 stoichiometric ratio of BTBP to ^{227}Ac with three nitrate ions for charge balancing as demonstrated by experimental analysis. The computed stability constants coupled with the vectorized information from the optimized BTBP molecular geometries were used for the training of ML workflows. The performance of each algorithm was determined by the validation set and the outcomes compared to the DFT stability constants. This methodology can aid radiochemists in synthesizing targeted ligands for selective isolation of ^{227}Ac.

Received 6th January 2025
Accepted 6th March 2025

DOI: 10.1039/d5dd00007f

rsc.li/digitaldiscovery

Introduction

Targeted α-therapy (TAT) is a promising radiotherapeutic technique for the treatment of various cancers.[1–8] The effectiveness of TAT is due to the high linear energy transfer (50–230 keV μm^{-1})[1,9] and the short path lengths (50–100 μm)[1] of α particles (^{4}He nucleus) allowing for the destruction of cancer cells in a confined region leaving healthy cells relatively unaffected.[1,2,5,9] There are, however, only a select few α-emitters that are able to be used for TAT since the α-emitters need a half-life long enough to be effective and cannot contain daughters that emit γ rays but ideally contain daughters that also emit α particles.[10] Of the acceptable radioisotopes for radiopharmaceutical applications, ^{223}Ra ($t_{1/2}$ = 11.4 d),[1,5,7,11] ^{224}Ra ($t_{1/2}$ = 3.6 d),[9,10] ^{225}Ra ($t_{1/2}$ = 14.9 d),[9] and ^{225}Ac ($t_{1/2}$ = 9.9 d)[1,2,6,9,10] are of interest due to their origination from ^{227}Ac,[12] the longest-lived, naturally occurring actinium isotope ($t_{1/2}$ = 21.77 years) being a great-granddaughter of ^{235}U.[3,13] Indeed, the first and only radioisotope currently approved by the FDA is ^{223}Ra in the form of $^{223}RaCl_2$ (Xofigo, Bayer HealthCare Pharmaceuticals)[11] for the treatment of prostate cancer. This radioisotope is known to be produced through the isolation of ^{227}Ac and ^{227}Th.[14] There are other methodologies for the production of ^{225}Ac,[3,4,6,7,9,15–17] where each of these processes involves the ^{227}Ac radioisotope whether directly from legacy sources or from the transmutation of ^{226}Ra, emphasizing the focus of this study on ^{227}Ac extraction. The radioisotope ^{225}Ac is also a promising α-emitter since the daughters of ^{225}Ac are also all α-emitters, allowing for increased radiation dosage to the cancer cells.[1,17,18] However, one of the major hindrances to the implementation of TAT is the supply of α-emitting radioisotopes.[4,9,17,18]

An alternative method for the extraction of actinide(III) radioisotopes is by solvent-based extraction with 6,6′-bis(1,2,4-triazin-3-yl)-2,2′-bipyridine (BTBP, Fig. 1A) ligands.[19–24] These ligands were designed for the selective extraction of trivalent actinides over trivalent lanthanides from a nitric acid medium.[19,23] They were also designed to be more resistant to radiation degradation than the 2,6-bis(1,2,4-triazin-3-yl)-pyridine (BTP) ligands.[19] The BTBP ligands coordinate to trivalent actinides in a 1 : 2 (actinide-to-ligand) ratio with instances of extraction in nitric acid solution possessing a coordinated nitrate ligand in the inner coordination sphere with the remaining charge balancing nitrates in the outer solvation

Department of Chemistry, University of Tennessee, Knoxville, Tennessee 37996-1600, USA. E-mail: kvogiatz@utk.edu

† Electronic supplementary information (ESI) available. See DOI: https://doi.org/10.1039/d5dd00007f

 © 2025 The Author(s). Published by the Royal Society of Chemistry

Open Access Article. Published on 14 March 2025. Downloaded on 1/8/2026 1:14:21 AM.
This article is licensed under a Creative Commons Attribution-NonCommercial 3.0 Unported Licence.

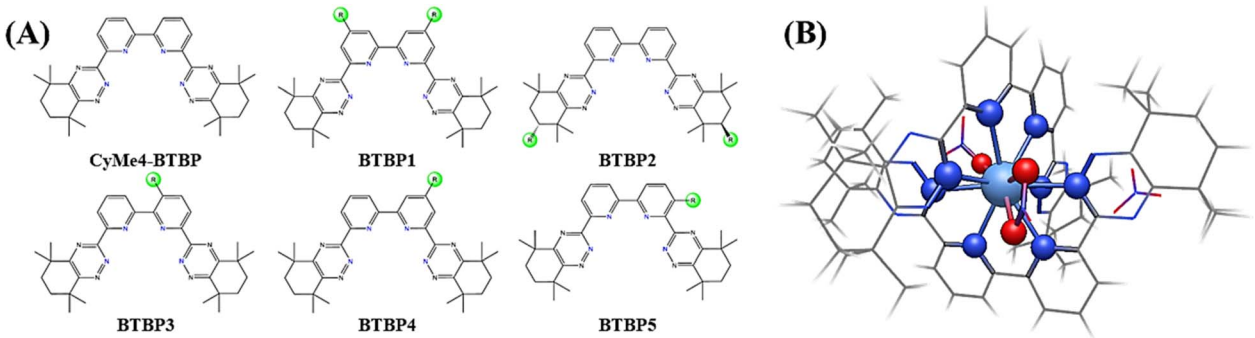

Fig. 1 (A) The reference **CyMe$_4$–BTBP** ligand and the five analogs labeled **BTBP1–BTBP5** considered in this study. Nitrogen atoms in blue font demonstrate the coordination sites of the BTBP ligands, R groups represent the substitution position(s) of the molecules. (B) Optimized geometry of the [Ac(**CyMe$_4$–BTBP**)$_2$(NO$_3$)$_2$]$^+$NO$_3^-$ coordination complex. The first coordination sphere of Ac(III) is shown as spheres (color code: light blue = Ac(III), red = O, blue = N, grey = C, and white = H).

sphere of the coordinating complex (Fig. 1B).[19,20,25] Extractions with selected BTBP complexes have been shown to be diluent dependent and importantly, structurally dependent. For example, extractions with 6,6′-bis(5,6-dipentyl-[1,2,4]triazin-3-yl)-[2,2′]bipyridine (**C5-BTBP**) were shown to be dependent upon the utilized diluent showing an increase in the distribution ratios between Am(III) and Eu(III) with an increase in the dielectric constant of the diluent.[19,26] Likewise, 6,6′-bis(5,5,8,8-tetramethyl-5,6,7,8-tetrahydro-benzo-1,2,4-triazin-3-yl)-2,2′-bipyridine (or **CyMe$_4$–BTBP**, in short), the current trivalent actinide/lanthanide extraction European reference ligand,[27] when used for extraction in 1-octanol/kerosene and 1-octanol of Am(III) and Eu(III), were shown to indeed selectively extract Am(III) over Eu(III). Unfortunately, the kinetics of these extractions were shown to be inadequate to justify industrial applications.[19,28]

Structural modification of BTBP ligands plays an important role in the optimization of actinide extractions.[19] As an example, Cm(III) and Eu(III) extractions were evaluated with **CyMe$_4$–BTBP** in methanol/3.3 mol% water using TRLFS[20] which demonstrated conditional stability constants (log β) of 12.4 ± 0.3 and 11.3 ± 0.3, respectively, while **C5-BTBP** in 1-octanol/water/0.04 M nitrate using TRLFS[19,29] was shown to be 10.8 ± 0.6 and 9.4 ± 0.4, respectively. Another study focused on the synthesis of two BTBP molecules (Cl–**CyMe$_4$–BTBP** and Br–**CyMe$_4$–BTBP**) with the halogen substituted on the *para* carbon with respect to the coordinating nitrogen atom on one of the bridging pyridine groups.[22] Comparing the behavior of both of these ligands to each other for Am(III) separations from Eu(III) demonstrated a maximum separation factor[20,30] of 124 ± 12 and 112 ± 11 at 3 M HNO$_3$ for Cl–**CyMe$_4$–BTBP** and Br–**CyMe$_4$–BTBP**, respectively.[22] This demonstrates that small structural changes in the functionalization of BTBP ligands can significantly affect the binding affinity of the BTBP ligands to actinides (actinium in this study) and the need to have a protocol for the screening of thousands of different BTBP ligands for evaluation can be vital towards separation optimization and ligand discovery.

Since current industrial processes utilize ligands, in the form of resins, for the selective separation of Ac(III) from a mixture of different isotopic quantities of Th(IV) and Ra(II) dissolved in nitric acid, solvent-based extraction methods have the potential to selectively separate Ac(III) from a mixture of impurities by utilizing highly selective BTBP ligands in the organic phase for Ac(III) separations while utilizing a masking agent that can be used to reduce divalent impurities (such as Ra(II))[19] from being extracted or a secondary ligand, such as the hydroxypyridinonate 3,4,3-LI(1,2-HOPO) ligand,[31] that can be used to selectively extract tetravalent impurities (such as Th(IV)). Indeed, one such ligand utilized in resin-based extraction is the *N*,*N*,*N*′,*N*′-tetraoctyl diglycolamide (TODGA)[9,18] ligand which has been explored in solvent-based separation processes with **CyMe$_4$–BTBP** for SANEX applications.[19,32] Utilizing solvent-based extractions as an alternative method for the extraction of ^{227}Ac could reduce the number of processes providing a simpler extraction process that can assist in the development of novel methods for extracting trace amounts of Ac found in the ocean,[33] uranium ore during the uranium processing stage instead of leaving it to decay, and from nuclear waste.[34] This would be advantageous for assisting in an increase in radioisotope supply for applications in targeted radiotherapy.

Artificial intelligence and machine learning (ML) methodologies have shown promise in the analysis and prediction of actinide properties and rare-earth element separations.[35–45] A recent study utilized ML to make thermochemical binding predictions from computational data of La(III) and Ac(III) with carboxylic acids.[45] More specifically, this study utilized supervised ML methods based on decision tree regression to predict ΔG_{rxn} values for the complexation of La(III) and Ac(III) with carboxylic acids by using Coulomb matrices of the coordinated complexes with inner shell coordination of solvent molecules (water). The most accurate results acquired in this study, in terms of mean absolute error (MAE), derived from the XGBoost[46] method resulted in a MAE of 6.93 kcal mol^{-1}.[45] Overfitting was observed in all the ML models trained in this study, which was hypothesized to be reduced upon the addition of a larger dataset. Liu and coworkers developed ML models for the prediction of log *D*, which is the logarithm of the distribution ratio, acquired from experimental analysis for lanthanide separations.[43] This study utilized fully connected neural networks with the extended-connectivity fingerprints[47] and a descriptor input vector extracted

Open Access Article. Published on 14 March 2025. Downloaded on 1/8/2026 1:14:21 AM.
This article is licensed under a Creative Commons Attribution-NonCommercial 3.0 Unported Licence.

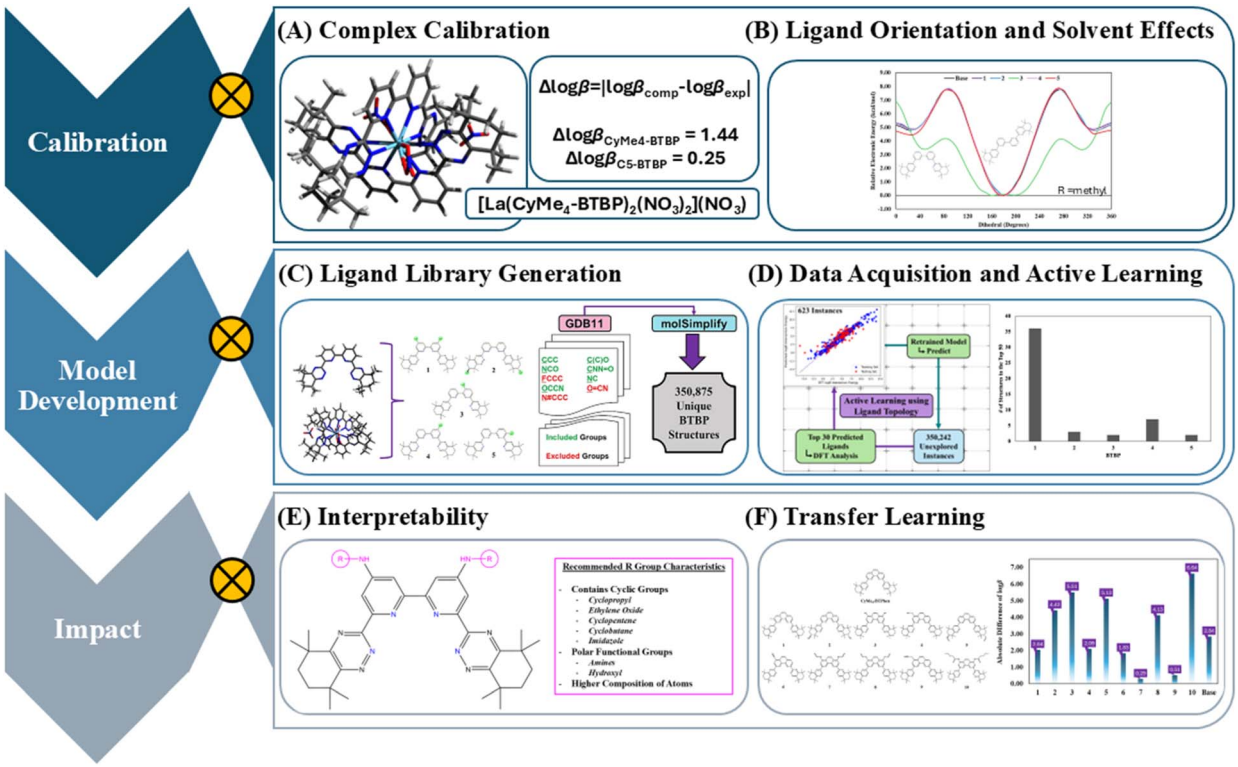

Fig. 2 Schematic overview of the individual steps considered in this study. The methodology calibration includes (A) examination of the coordination complex with the assistance of experimental data and (B) the orientation and solvation effects of the BTBP analogs using dihedral rotations with methyl groups as substituents. The model development focuses on (C) the generation of the ligand library that was used for this study and (D) the collection of stability constants (log β) for the initial dataset used for training the machine learning algorithm. The active learning process enabled us to augment the training dataset by taking the top 30 performing ligands as predicted by ML and computing their respective log β value. The model's impact is evaluated based on (E) the interpretability from the ML results to provide targeted functional groups that were computationally predicted to improve ^{227}Ac complexation and (F) transfer learning where predictions were made on 10 + 1 **CyMe$_4$–BTPhen** ligands using ML algorithms trained with BTBP ligands.

by RDKit[48] for the individual ligands and the log D values with their respective experimental conditions such as temperature and concentration as examples, as inputs for the neural network. From this study, they were able to acquire a MAE of 0.34 and a root mean square error of 0.53 for their validation set.[43] Both studies have specific limitations but are relevant to our study as we aim towards thermochemical predictions based on the structure of the ligand to generate a simple method for screening unexplored ligands for ^{227}Ac extractions.

The present study explores ^{227}Ac extractions using **CyMe$_4$–BTBP**-based variants as an alternative to current industrial processes and provides a general methodology for BTBP-based ligand discovery and design through scalar relativistic density functional theory (DFT) and ML. We have considered ligand featurization that utilizes information from molecular topology and electronic structure. The workflow for this study is graphically illustrated by Fig. 2 which highlights the three major sections that are presented and discussed: calibration, model development, and impact of the ML results. Application of active learning enabled an extended and reliable screening of thousands of unexplored functionalized BTBP analogs. The interpretability of the ML methodology presented here, as well as its transferability to functionalized **CyMe$_4$–BTPhen** ligands, is discussed.

Results

Ligand library development

The aim of this study was the effective prediction of log β values for more than 350 000 molecular units using only the BTBP ligand geometries and without performing expensive geometry optimization of the full complex (2 : 1 ratio between the ligand and actinide cation). This was achieved by using DFT-generated data from a small subset of the full ligand library. In particular, a ligand library of 350 875 unique molecular structures were generated (see Computational details). Each class of atom size functional groups with respect to SMILES strings has approximately equal amounts of **BTBP1–5** generated. Hereafter, when discussing the atom size of a functional group it will be implying the size of the SMILES string which excludes the hydrogen atoms. The five different families that were used for the generation of the ligand library included two families that were symmetrically functionalized and three that were asymmetrically functionalized (Fig. 1A). The two symmetrical families involved the functionalization of the *para* sites of the 2,2′-bipyridine unit of the **CyMe$_4$–BTBP** scaffold with respect to the coordinating N atoms (**BTBP1**), and the functionalization of the lower C atom that is positioned between the tetramethyl substituted cyclohexene unit of the scaffold (**BTBP2**). The

 © 2025 The Author(s). Published by the Royal Society of Chemistry

Open Access Article. Published on 14 March 2025. Downloaded on 1/8/2026 1:14:21 AM.
This article is licensed under a Creative Commons Attribution-NonCommercial 3.0 Unported Licence.

asymmetric functionalization included the single substitution of one side of the 2,2′-bipyridine portion of the **CyMe$_4$–BTBP** scaffold by substitution of the *meta* site with respect to the coordinating N atom closest to the other half of the 2,2′-bipyridine group (**BTBP3**), substitution of the *para* site (**BTBP4**), and substitution of the other *meta* site, which is closest to the 1,2,4-triazine group of the BTBP scaffold (**BTBP5**).

Ligand orientation and complexation calibration

Before the generation of the necessary data, we first wanted to determine the most stable conformation of the BTBP ligands (ESI, Section S1†) and the Ac(III) complexation with BTBP. The most probable Ac(III) complexation was determined by using La(III) for select ligand complexation analysis due to its chemical similarity to Ac(III).[45,49] This was accomplished by taking known experimental log β values of La(III) ligation since, to the best of our knowledge, Ac(III) has no known experimental log β values for these systems. This calibration allowed us to make inferences about the expected performance of Ac(III) ligation with BTBP ligands.

Table 1 demonstrates experimental log β values for the 1 : 2 ratio of Cm(III) (from our previous study,[50] shown here for comparison) and La(III) using different BTBP ligands. The log β values were computationally determined from the chemical reactions (R1) and (R2) for the complexation with Cm(III) and La(III), respectively (L represents the BTBP variants). The coordination complex for La(III) was shown to have an additional nitrate ligand coordinated to the nuclide than Cm(III). Since in our previous study we found agreement between the DFT optimized coordination complex with spectroscopic experimental observations of Cm(III) having a single nitrate ligand coordinated to the complex,[19,20,50] we could then imply that due to the larger atomic radius, La(III) could allow for a larger coordination number as determined by DFT. We also note that the predicted log β values for La(III) were overall in better agreement with the experimental values than the Cm(III) values. Thus, we infer that due to the chemical similarity between La(III) and Ac(III), that the log β values from our computational protocol should provide reasonable agreement with the actual value from future experiments.

$$Cm(NO_3)_3 + 2L \rightarrow [Cm(L)_2(NO_3)]^{2+}(NO_3)_2^{2-} \quad (R1)$$

$$La(NO_3)_3 + 2L \rightarrow [La(L)_2(NO_3)_2]^{+}NO_3^{-} \quad (R2)$$

Table 1 Selected experimental stability constants compared to computationally determined stability constants for Cm(III) and La(III) ligation with BTBP ligands

Structure	M(III)	Experimental log β	Computed log β	Δlog β
***t*-Bu–C2–BTBP**	Cm	11.1 ± 0.15[a]	14.52[d]	3.42
CyMe$_4$–BTBP	Cm	12.4 ± 0.3[b]	13.14[d]	0.74
	La	8.8 ± 0.1[c]	10.24[e]	1.44
C5-BTBP	La	10.0 ± 0.3[c]	9.75[e]	0.25

[a] From ref. 30. [b] From ref. 20. [c] From ref. 51. [d] From ref. 50. [e] This work.

We then used computationally determined stability constants and electronic energies to evaluate the trends from rotations about dihedral angles of **CyMe$_4$–BTBP** as well as substituted **CyMe$_4$–BTBP** analogs. The full discussion on dihedral rotation can be found in the ESI (Sections S1 and S2)† and our key findings are summarized here. First, we evaluated the log β associated with Ac(III) ligation with each BTBP analog (Fig. 1A) using methyl as the substituent and then computed the energy barrier between all BTBP conformations of the individual analog to compare thermodynamic favorability with respect to the rotational barriers. Analysis of the computed log β for these analogs demonstrated the following trend from most favorable to least favorable: **CyMe$_4$–BTBP** > **BTBP2** > **BTBP4** > **BTBP1** > **BTBP5** > **BTBP3**. Comparison of the log β values with respect to the energy barrier of the BTBP analogs demonstrated that the thermodynamic stability constants are dependent upon the coordination complex itself and are not affected by complexation kinetics that are dependent upon the organizational penalty. This phenomenon was observed experimentally when comparing the experimentally determined log β for La(III) with the formation rate constant, which was too rapid of a reaction to acquire interpretable results for **CyMe$_4$–BTPhen**, whereas **CyMe$_4$–BTBP** was measured to be 70.5 ± 0.8 L mol^{-1} s^{-1} with the stability constants for **CyMe$_4$–BTBP** (8.6 ± 0.2) and **CyMe$_4$–BTPhen** (8.5 ± 0.2) in acetonitrile showing only a difference of 0.1 for these relatively similar ligands.[52]

To elucidate the solvation effects on the selective complexation between Ac(III) and La(III), the separation factor (SF) for La(III)/Ac(III) ligation using **CyMe$_4$–BTBP** was evaluated since it has been shown experimentally that the SF increases with decreasing relative permittivity of the solvent when analyzed with Am(III)/Eu(III) separations.[23] We also chose to compare Ac(III) with La(III) as the separation between these two radionuclides would be the most challenging if La(III) is present in an analyte with Ac(III). $SF_{La(III)/Ac(III)}$, the ratio of the $\beta_{M(III)}$[30] values, was calculated using eqn (1):

$$SF_{A/B} = \frac{10^{\log \beta_A}}{10^{\log \beta_B}} = \frac{\beta_A}{\beta_B} \quad (1)$$

Interestingly, $SF_{La(III)/Ac(III)}$ was shown to have the opposite effect for the following $SF_{La(III)/Ac(III)}$ values with the solvent and their respective relative permittivity in parentheses: 5024.52 (methanol, 32.63), 1976.47 (water, 80.4), 793.32 (1-octanol, 10.3), and 2.58 (kerosene, 1.998). This inverse in the behavior demonstrated by Am(III)/Eu(III) separations can be summarized by stating that in general the SF decreases with decreasing relative permittivity between La(III) and Ac(III); however, methanol was an exception providing the highest SF value out of the four solvents. Indeed, water, which has a higher relative permittivity value than methanol, resulted in a significantly smaller SF. This computational finding implies that optimizing the SF between specific actinides and lanthanides requires solvent dependent investigations. These results also demonstrate that the commonly used kerosene in industrial applications would be ineffective at removing Ac(III) from La(III) and instead methanol should be utilized since it possessed the highest SF value.

Open Access Article. Published on 14 March 2025. Downloaded on 1/8/2026 1:14:21 AM.
This article is licensed under a Creative Commons Attribution-NonCommercial 3.0 Unported Licence.

Data collection

We began this study with the consideration of a small subset of 623 ligands evaluated with DFT from this library. We followed a bottom-up procedure where the initial data were collected from molecular geometries of BTBP variants with small functional groups, with the aim of developing ML models that predict properties of larger molecular structures. More precisely, we have utilized all BTBP variants with substituents consisting of 1, 2, 3, and 4 non-hydrogen atoms, together with a small subset of substituents with 5 non-hydrogen atoms. The total number of the selected ligands was 640. DFT computations were performed to determine the $\log \beta$ values of each ligand in this subset, but 17 computations were not completed successfully and were returned to the ligand library. Thus, a total of 623 DFT data were used for training a ML algorithm for making predictions on the full ligand library (Fig. 3). A full breakdown on the distribution of the datasets utilized in this study can be found in the ESI (Section S4 and in Fig. S8).†

A short analysis was carried out on the 50 molecular complexes with the highest computed $\log \beta$ values (out of the initial 623 examined by means of DFT). We note some common features present in the functional groups of these top 50 ligands, such as 27 of the top 50 contain amine groups, 12 contain a hydroxyl group, 6 contain a cyclic group, and 4 contain a carboxyl group (ESI, Section S3†). These results demonstrated that the addition of polar groups increases the favorability for complexation with Ac(III) since only two ligands out of 50 contain nonpolar functional groups (cyclobutyl). We also identified the symmetrical **BTBP1** and the asymmetrical **BTBP4** ligand scaffolds as the preferable functionalization sites. In both cases, the substituent is in the *para* site with respect to the coordinating nitrogen of the 2,2′-bipyridine group within the BTBP analog.

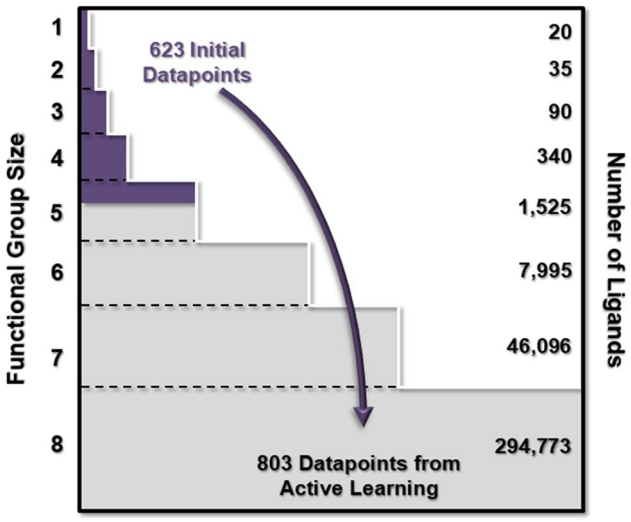

Fig. 3 Schematic representation of the bottom-up active learning process followed in this study. An initial subset of 623 ligands (including the parent BTBP ligand) with a functional group size of 1, 2, 3, 4, and 5 non-hydrogen atoms was used as the initial set for ML model training (space shown in purple) out of a total of 350 874 generated ligands. These 350 874 ligands were successfully generated from the parent BTBP ligand by using SMILES strings with non-hydrogen atom numbers of 1 through 8. This approach allowed us to organize and monitor the different ligand sizes and their performance with ^{227}Ac ligation. Active learning steps systematically increased the training set with data from molecular units with a larger functional group (5, 6, 7 or 8 non-hydrogen atom substituents). The number of ligands for each functional group size is given at the right, figure not to scale.

High-throughput virtual screening *via* active learning

A major objective of this study was to provide the tools necessary for the screening of unexplored BTBP ligands for the prediction of reliable $\log \beta$ values. The computational workflow presented here avoids the explicit computation of each molecular complex (350 875 in total) by means of DFT and active learning, which can provide directions for the targeted synthesis of the next generation of BTBP-based ligands. For that purpose, we utilized the computational data collected from the 623-ligand dataset and progressively increased the size of the ligand dataset in each active learning step (Fig. 3). The active learning process included the following phases: training, database screening, validation, data augmentation, and retraining. The model trained on the 623-ligand dataset was used for screening the unexplored 350 242 ligand dataset, and predicted $\log \beta$ values were obtained for each molecular unit.

The validation of these predictions was performed by using a validation set composed of 10 randomly selected structures from the remaining 350 252 unexplored molecules. Of these 10 BTBP ligands, six consisted of functional groups with an eight-atom scaffold, two contained seven, and two consisted of functional groups with a five-atom scaffold (see ESI S5† for more details). Three of the BTBP ligands were members of the **BTBP1** analog, four were of the **BTBP2** analog, one was from the **BTBP3** analog, and two were from the **BTBP5** analog. We first optimized the geometry of all 10 structures and then determined the $\log \beta$ values computationally to then be used as comparisons for the predictability of the trained algorithms on new ligands. Note that the validation set was kept unchanged during the active learning steps to track the performance and the increased accuracy of the retrained models (*vide infra*).

Active learning is a machine learning technique that iteratively improves a model by identifying and incorporating new data points where predictions are uncertain. If a model's predictions deviate significantly, new data are added to the training set, the model is retrained, and the process repeats until convergence or predefined criteria are met. In this study, active learning was implemented by selecting 30 ligands with the highest predicted $\log \beta$ values from an extended, unexplored ligand library to augment the dataset. Additional DFT geometry optimizations were performed for the full molecular complexes with these 30 additional ligands, new $\log \beta$ values were computed, and comparisons between the ML and DFT $\log \beta$ values were used as an additional control of the models' performance (a detailed discussion on the active learning steps and the collected data is provided in ESI Sections S6–S8†). The

 © 2025 The Author(s). Published by the Royal Society of Chemistry

Open Access Article. Published on 14 March 2025. Downloaded on 1/8/2026 1:14:21 AM.
This article is licensed under a Creative Commons Attribution-NonCommercial 3.0 Unported Licence.

predicted log β values for each of the 10 molecules of the validation set with respect to the actual DFT values are shown in Fig. 4, while the inset demonstrates the improved predictability as the training dataset increased from the initial 623-ligand instances to the 803-ligand dataset, after 6 active learning steps. The grey arrows show the shift of the predicted values during the active learning steps. For example, we identified three outliers that are located in the upper right region of the plot and have significantly higher DFT values (log β is 10 or higher). These three cases belong to the **BTBP1** family of functionalized ligands, and they are shown in ESI S5, Fig. S9.† As the ML models are trained with more data (from 623 to 803), the model's accuracy is increased, as is shown with the value shift towards the diagonal. We also note that similar behavior was found for the rest of the validation set. The drop shown in the inset of Fig. 4 (between dataset 713 and 743) further demonstrates the improvement in the model with a Δlog β value of 0.84 which corresponds to 4.79 kcal mol^{-1} uncertainty. We also quantified the performance of each dataset by calculating the mean absolute error (MAE, which can also be found in the inset of Fig. 4 as previously discussed) and root mean square error (RMSE) for the 623-ligand dataset (MAE of 3.05 and RMSE of 4.23), the 653-ligand dataset (2.99 and 4.04, respectively), the 683-ligand dataset (3.04 and 4.12, respectively), the 713-ligand dataset (3.01 and 3.77, respectively), the 743-ligand dataset (2.17 and 3.06, respectively), the 773-ligand dataset (2.50 and 3.30, respectively), and the 803-ligand dataset with a MAE value of 2.42 and a RMSE value of 3.28.

To further elucidate the predictability improvement during the active learning steps, we report the evolution of the data distribution, as we augmented the training set from 623 instances (ESI S8 Fig. S11, top†) to 803 instances (ESI S8 Fig. S11, bottom†). The 5 different families of ligands are organized into 5 groups based on their log β values, *i.e.* below 0, between 0 and 5, between 5 and 10, between 10 and 15, and above 15. We highlight that the distribution associated with the **BTBP1** analog demonstrated that before the inclusion of the active learning molecules, there were no reported log β values above 15, whereas active learning provided 24 **BTBP1** ligands with a log β value above 15. This assisted in improving the predictability of the validation set since the two significant outliers were both **BTBP1** analogs with stability constants above 15. We also note the increase in ligands with a log β value in the 10–15 range by 59 during the active learning process for the **BTBP1** analog. Thus, active learning helped the model to adapt and be trained on datapoints with higher log β values improving the validation set performance.

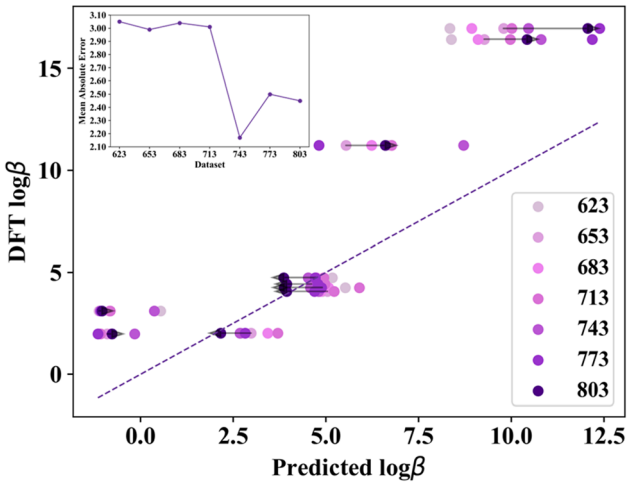

Fig. 4 Parity plot between the DFT and the predicted log β values from the ML models trained during the data augmentation from active learning. The legend shows the color code corresponding to the different training set sizes. The grey arrows demonstrate the evolution of the log β values during the active learning process. The inset graph demonstrates the learning curve of the 10-molecule validation dataset with respect to the mean absolute error of the predicted and DFT log β values starting from the initial 623-ligand dataset to the 803-ligand dataset with each of the active learning steps in between.

The active learning process also identified that symmetrically functionalized BTBP ligands significantly improve ^{227}Ac complexation (**BTBP1** and **BTBP2** families). From the 623 ligands of our initial dataset, 20 **BTBP1** and 3 **BTBP2** variants had a log β value above 10, while after the four active learning steps, these numbers increased to 103 and 7 variants from the **BTBP1** and **BTBP2** families, respectively. The top-10 performing ligands discovered by active learning are presented in Fig. 5. All ligands are symmetrical, they belong to the **BTBP1** family and contain functional groups that are bonded to the BTBP scaffold through a nitrogen atom (with the exception of ligand 664 that is connected through a carbon atom). Additional observations include that these ligands contain (a) cyclic functional groups (ligands 769, 785, and 792 are exceptions), (b) at least one double bond (ligands 774 and 795 are exceptions), and (c) contain polar functional groups. These functional groups are all composed of 8 atom scaffolds (excluding H atoms).

Finally, we provide a set of recommendations for the functional groups and functionalization site (Fig. 6) based on analysis of the ligand characteristics that produced high log β values for ^{227}Ac complexation in methanol. We first note the preferred functional site of the BTBP analogs studied in this work. We found that the symmetrical *para* positions of the coordinating nitrogen atoms of the 2,2′-bipyridine group enhance the ligation with actinium. The recommended R groups providing the largest log β values from this study are shown on the right side of Fig. 6 in the magenta box. Our first recommendation is to bridge the BTBP scaffold to the functional group by using an –NH– linker coordinated to the BTBP core. This was a characteristic demonstrated by nine of the top ten ligands. The rest of the functional group branching from the amine bridge has several recommendations for design. The first is the use of cyclic groups such as cyclopentene, cyclopropyl, ethylene oxide, cyclobutane, and imidazole groups. We also recommend minimally branched functional groups, such as a single branch from the linear chain with minimal steric strain. The presence of double bonds was observed to be significant as well, being present in eight of the top ten ligands with a maximum of two double bonds being observed in a functional group. The functional groups should also be polar and contain oxygen and nitrogen groups, especially hydroxyl groups that were in eight of

Open Access Article. Published on 14 March 2025. Downloaded on 1/8/2026 1:14:21 AM.
This article is licensed under a Creative Commons Attribution-NonCommercial 3.0 Unported Licence.

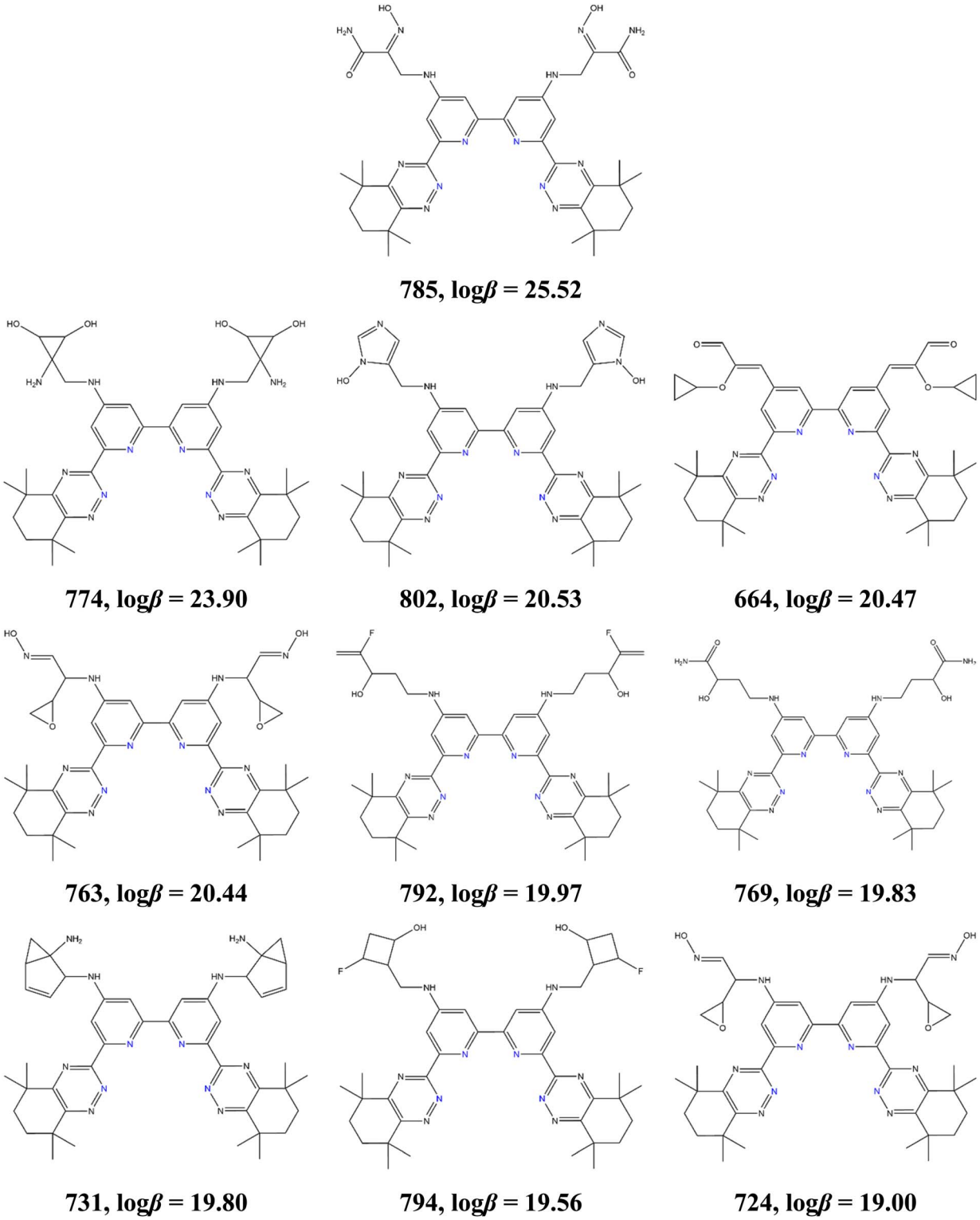

Fig. 5 The top ten ligands out of the 803 ligands analyzed through this study and their log β values computed by DFT.

the ten ligands. Finally, we observed that functional groups containing a higher composition of atoms provided stronger favorability for ^{227}Ac complexation than when functionalized with smaller functional groups.

Transfer learning

Lastly, we evaluated whether the trained model could make predictions on the structurally similar BTPhen-based ligands on ^{227}Ac complexation. To do so, we used the ML model

 © 2025 The Author(s). Published by the Royal Society of Chemistry

Open Access Article. Published on 14 March 2025. Downloaded on 1/8/2026 1:14:21 AM.
This article is licensed under a Creative Commons Attribution-NonCommercial 3.0 Unported Licence.

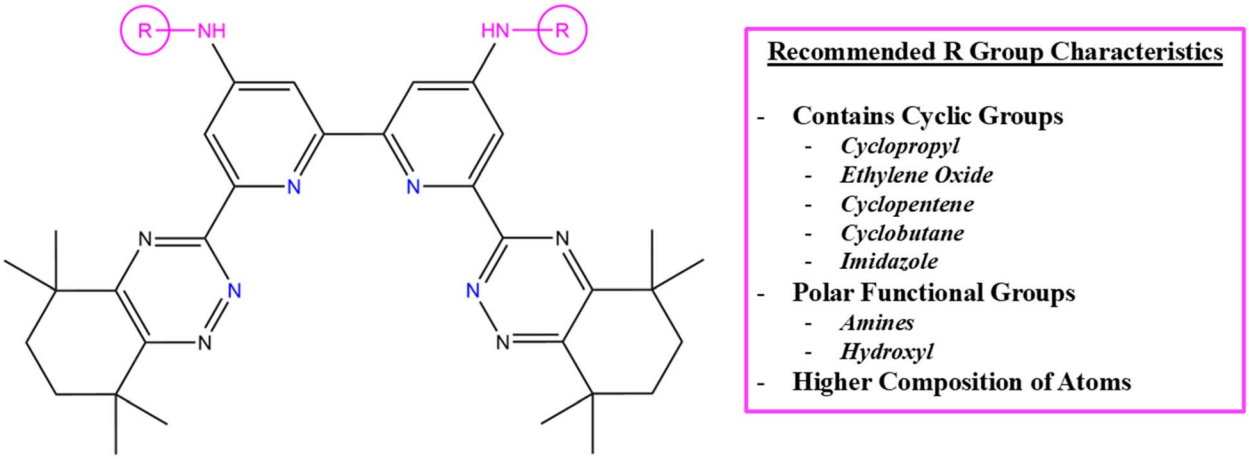

Fig. 6 Proposed ligand design for synthesizing ligands to optimize ^{227}Ac extractions in methanol determined from this study. The functional group design is demonstrated in the magenta box and the preferred functional sites are demonstrated by the magenta functional groups.

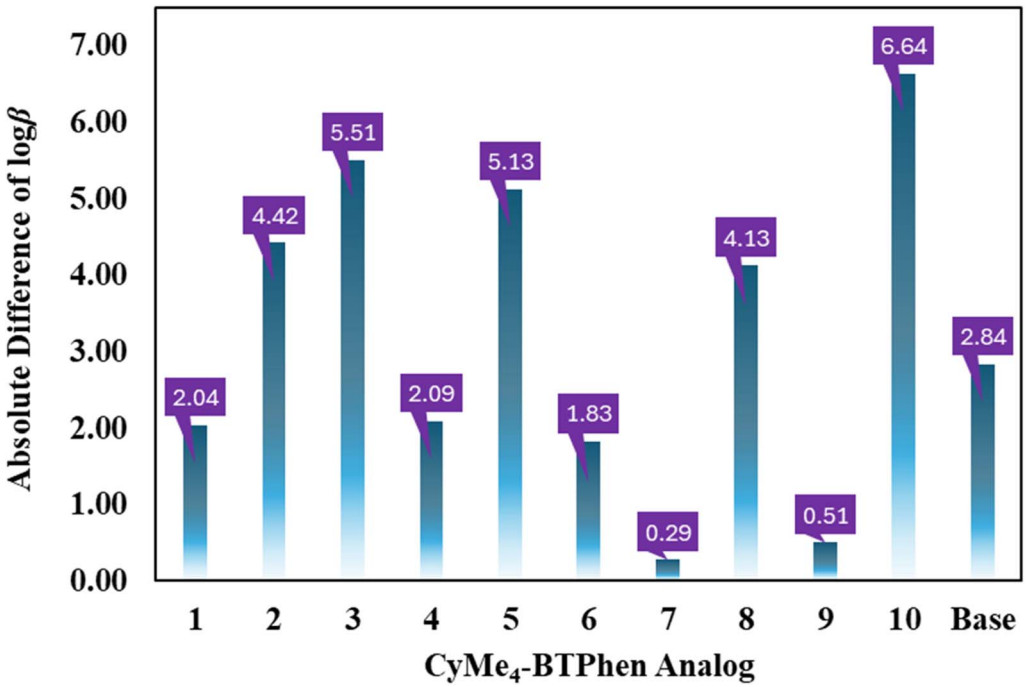

Fig. 7 Transfer learning results using the model trained on 803 BTBP ligands for predicting log β values of 10 + 1 **CyMe$_4$–BTPhen** analogs (their structures are shown in ESI Section S5 and Fig. S10†). The y-axis shows the absolute difference between the DFT-computed and the predicted log β values.

trained on the DFT optimized 803-ligand dataset to predict log β values of the BTPhen parent ligand together with 10 BTPhen variants using only their molecular structure (and not the full coordination complex) which are shown in ESI S5, Fig. S10.† The resulting absolute differences in log β values with respect to the DFT computed values and the predicted values from the trained ML algorithms are demonstrated in Fig. 7. To evaluate model performance, the mean absolute error (MAE, 3.22) and the root mean square error (RMSE, 3.79) between the DFT and predicted log β value are also reported. These error values are in good agreement with the final active learning step involving only BTBP ligands (the 803-ligand dataset) which had a MAE of 2.42 and a RMSE of 3.28 and thus, both models have comparable uncertainty. Since DFT-optimized BTBP ligands were used, the DFT optimized BTPhen-based ligands were also used for making predictions. Overall, we found that for the prediction of BTPhen molecules, an algorithm trained on DFT optimized BTBP ligands can provide reasonable agreement for the expected DFT stability constants without the computation of the computationally demanding coordination complexes.

Open Access Article. Published on 14 March 2025. Downloaded on 1/8/2026 1:14:21 AM.
This article is licensed under a Creative Commons Attribution-NonCommercial 3.0 Unported Licence.

Conclusions

The *in silico* optimization of the tetradentate BTBP ligands for enhancing ligation with ^{227}Ac using active learning and ligand topology was discussed in this article. The study involved three stages: calibration, model development, and chemical interpretation. The calibration included the molecular complex ligation and the consideration of the correct coordination environment between two BTBP units and ^{227}Ac, conformation search of the bare ligand, and solvent effects. These tasks were important for the accurate modeling of the full molecular complexes by DFT.

A dataset of 350 875 unique BTBP variants was generated by considering 5 different functionalization sites, two of which generated symmetrical ligands (**BTBP1** and **BTBP2** ligand families) and three unsymmetrical (**BTBP3**, **BTBP4**, and **BTBP5** families). From these, we selected 640 ligands, and we computed their $\log\beta$ values by performing DFT geometry optimizations of the full complex (2 : 1 ratio between BTBP and ^{227}Ac). A curation step reduced the number of DFT data to 623 to ensure the reliability of the data used for the training of a ML model. In all ML models, we introduced topological information of the molecular ligands together with electronic structure features *via* a concatenated input vector (PI + SOAP). Then, we utilized active learning to predict $\log\beta$ values of the unexplored BTBP ligands in a systematic manner. This was accomplished in six active learning steps which were augmenting the ligand set with an additional 30 ligands, followed by extra DFT computations that determined the $\log\beta$ values. Following this procedure, we increased the dataset from 623 ligands to 803 ligands. The predictability of the trained models was evaluated by comparing the ML-generated $\log\beta$ values with respect to DFT for a separate set of 10 ligands (validation step). Analysis of the top performers led to the suggestion of ligand design principles. We concluded that the symmetrical **BTBP1** analog is the preferred class of ligands for ^{227}Ac extractions, with substituents that are coordinated to the BTBP body *via* an NH group (secondary amine).

We have also explored the transferability of the trained model to a different family of tetradentate ligands. The trained ML model on BTBP data showed good accuracy for a set of 10 + 1 **CyMe$_4$–BTPhen** derivatives. The importance of this becomes evident when considering that the only input information needed for the $\log\beta$ predictions is the optimized geometries of the bare ligands, an approach that surpasses the more time-consuming optimization of the larger molecular complexes ligated with ^{227}Ac cations. Therefore, this methodology can be used in the future for a large-scale study for the extraction of ^{227}Ac over Th(IV) and Ra(II) for either the optimization of the current leading extraction process with ion chromatography or for solvent-based methods. The results presented here demonstrate that solvent-based extractions of ^{227}Ac should be feasible, especially with the ligands that have $\log\beta$ values above 15, and based on the fact that Th(IV) would not favorably complex with BTBP molecules and Ra(II) interactions could be reduced by the use of a masking agent. We conclude that further optimization for the determination of the optimum ligand to use for Ac(III) would still need to be carried out as there is a vast number of unexplored ligands for Ac(III) complexation.

Computational details

Molecular structure database

A molecular library that includes five BTBP analog ligand classes used for functionalization to use for data generation and machine learning analysis was generated by using molSimplify[53] that applies OpenBabel[54,55] in the backend to create molecular substitutions. The substitutions were made at symmetrical and asymmetrical positions of a parent structure (**CyMe$_4$–BTBP**) creating five uniquely substituted BTBP molecule types (Fig. 1A). This was done by using a semi-automated refinement of the GDB8 database (subspace of the GDB11).[56,57] Each GDB8 entry is represented as a SMILES string. For example, structures that began with a F atom were excluded, since a terminal fluorine cannot coordinate to the parent structure. Thus, a total of 350 875 unique BTBP molecules were generated for this study. The distribution of the composition for the functional groups per molecular scaffold used for ligand substitution of the BTBP analogs is given in Table 2. Note that the sum of these generated ligands is not the sum of the total database by one ligand and that is simply due to the unsubstituted **CyMe$_4$–BTBP** ligand not being included.

Since the creation of the coordination complexes for Ac(III) with the individually functionalized BTBP molecules would be an arduous task, the same protocol was utilized for the creation of the Ac(III) 1 : 2 ratio BTBP complexes but with a pre-optimized $[\mathrm{Ac}(\mathbf{CyMe_4\text{–}BTBP})_2(\mathrm{NO_3})_2]^+\mathrm{NO_3}^-$ coordination complex (shown in Fig. 1B). The same molecular substitutions were used for the two BTBP molecules shown in this complex as those from Fig. 1A creating coordination complex counterparts to the individual BTBP molecules for further DFT calculations.

Ligand orientation – calibration

Dihedral analysis was accomplished by using the built-in scan function in ORCA 5.0 [58–60] to investigate the energy barriers of the different conformers of the **CyMe$_4$–BTBP** molecule and the BTBP analogs from Fig. 1 using methyl as the substituent. The energy barrier analysis utilized water, methanol, 1-octanol, and kerosene as solvents to show solvation effects on the organization and energy barriers of the BTBP ligands.[23,24,61] These energy barriers were calculated with respect to the most stable conformer (lowest electronic energy). Fig. 8A demonstrates the dihedral angles investigated in this study. The dihedral angle φ_1 was used for **CyMe$_4$–BTBP** as well as the methyl substituted

Table 2 Distribution of functional group scaffold composition used for ligand generation

Scaffold	1	2	3	4	5	6	7	8
Generated ligands	20	35	90	340	1525	7995	46 096	294 773

 © 2025 The Author(s). Published by the Royal Society of Chemistry

Open Access Article. Published on 14 March 2025. Downloaded on 1/8/2026 1:14:21 AM.
This article is licensed under a Creative Commons Attribution-NonCommercial 3.0 Unported Licence.

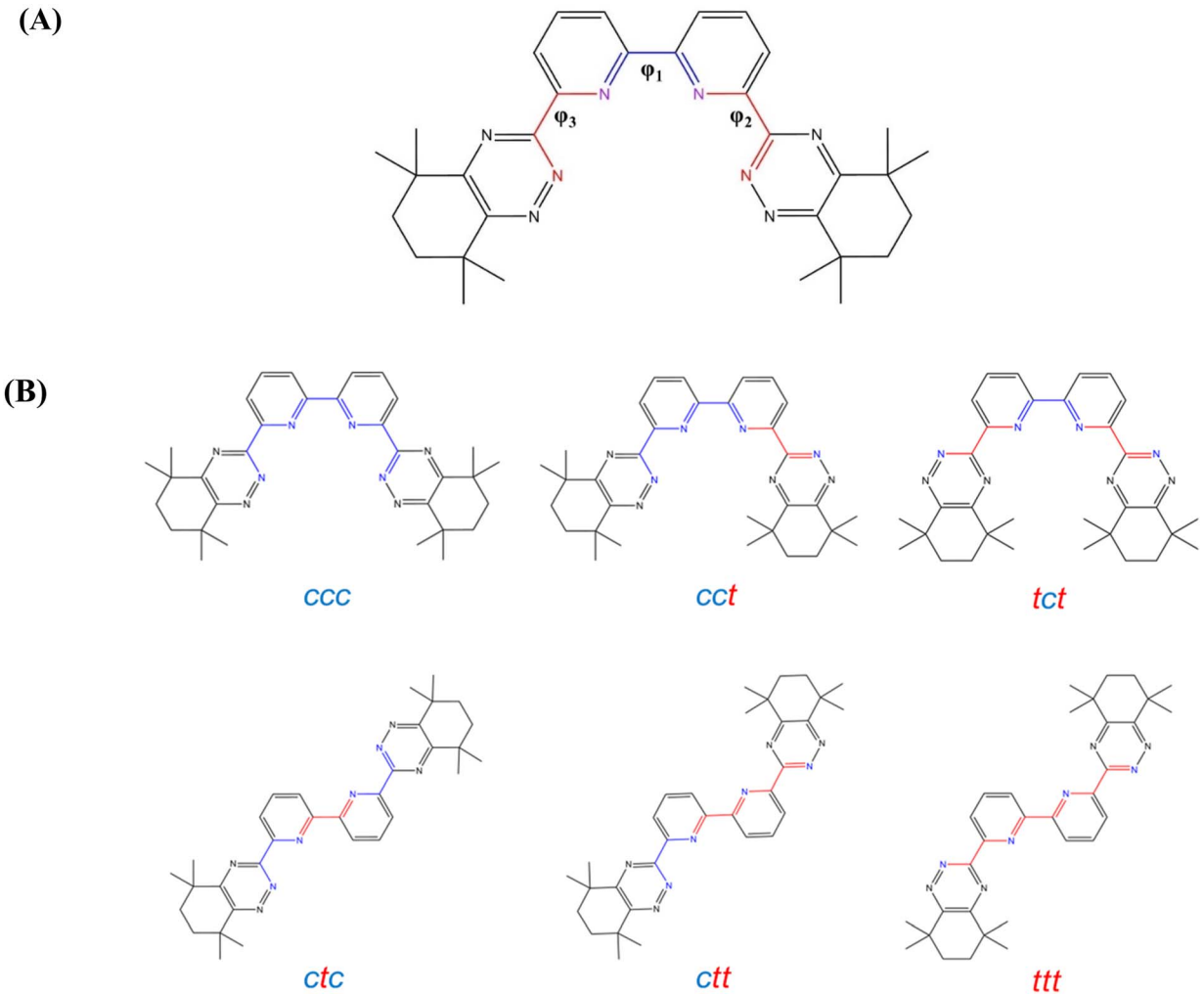

Fig. 8 (A) Labelled dihedral analysis for the BTBP ligands with **CyMe$_4$–BTBP** as an example. φ_1 (blue) shows the dihedral angle used for the rotation of the 2,2′-bipyridine group while the φ_2 and φ_3 (red) shows the dihedral angle for the rotations about the connecting dihedral between 2,2′-bipyridine and 1,2,4-triazine groups. (B) The six different conformers for the **CyMe$_4$–BTBP** ligand. The *cis* conformations are color coded as blue and the *trans* are red.

BTBP ligands to investigate the steric effects of the transitions between the *ctc* (*cis*, *trans*, *cis*) and the *ccc* conformers (Fig. 8B). The dihedral scan was performed with 10° intervals from 0° to 360° making 37 conformers of each ligand. An additional analysis was conducted for **CyMe$_4$–BTBP** which took each φ_1 conformer, fixed the dihedral, and did 37 scans at 10° intervals from 0° to 360° for φ_2 producing the *cct*, *ctc*, *ctt*, and *ccc* conformations, excluding the *ttt* and *tct* conformations. Further analysis was conducted by taking the minimum *ctt* and *cct* conformers along the path towards the most favorable *ccc* conformer of each potential energy surface and rotating the previously unrotated 1,2,4-triazine group (φ_3) by 180° at 10° intervals starting at 0° to analyze all possible BTBP conformers and acquire the full energy profile of each BTBP ligand.

Quantum chemical calculations

Density functional theory (DFT) computations were performed with the ORCA 5.0 quantum chemistry package[58–60] which allows the incorporation of scalar relativistic effects using the zeroth-order regular approximation (ZORA)[62] and the segmented all-electron relativistically contracted (SARC)[63] basis sets. The conductor-like polarizable continuum model (CPCM)[64] was utilized for the incorporation of solvation effects using the built-in solvents methanol, 1-octanol, and water. For kerosene, the dielectric constant and refractive index used were 1.998 and 1.44, respectively.[65] All molecular geometry optimizations used the BP86 (ref. 66 and 67) density functional with the SARC-ZORA-TZVP[63] basis set for Ac(III)/La(III), both with a closed-shell electronic structure, and the ZORA-def2-SVP[68,69] basis set for all other atoms. Each calculation also utilized the resolution of identity for the calculation of the two-electron integrals with the SARC/J auxiliary basis set. The quasi-harmonic approximation was used to compute the Gibbs' free energy at 298.15 K by the addition of the zero-point energy with the thermal vibrational-rotational entropies of the lowest-energy conformers using the same level of theory as the DFT geometry optimizations. This methodology has been used in

Open Access Article. Published on 14 March 2025. Downloaded on 1/8/2026 1:14:21 AM.
This article is licensed under a Creative Commons Attribution-NonCommercial 3.0 Unported Licence.

our previous studies where it provided good agreement between the computed and experimentally determined stability constants of Cm(III) ligation with **CyMe$_4$–BTBP** and ***t*-Bu–C2–BTBP**.[50,70]

Automated data curation was mandatory to screen the large number of calculations performed for this project. Any calculations that failed due to poor starting geometry or that finished but contained imaginary frequencies below $-50i$ cm^{-1} were filtered out of the useable structures for thermochemical analysis. The Gibbs' free energy values were utilized for the calculation of $\log\beta$ at a specific temperature T using (2).[19,71] The reaction used for this study for both Ac(III) as determined by the complexation calibration with La(III) is shown in (R3).

$$\Delta G = -2.303RT\log\beta \tag{2}$$

$$\mathrm{Ac(NO_3)_3} + 2\mathrm{BTBP} \rightarrow [\mathrm{Ac(BTBP)_2(NO_3)_2}]^{+}\mathrm{NO_3}^{-} \tag{R3}$$

Where β is computed as:

$$\beta = \frac{\left[\left[\mathrm{Ac(BTBP)_2(NO_3)_2}\right]^{+}\mathrm{NO_3}^{-}\right]}{\left[\mathrm{Ac(NO_3)_3}\right]\left[\mathrm{BTBP}\right]^2} \tag{3}$$

Machine learning

The machine learning input vectors utilized molecular descriptors of the individual BTBP ligands by using persistence homology[72,73] coupled with the smooth overlap of atomic positions (SOAP).[74,75] This involved the generation of persistence images (PIs) by the vectorization of persistence diagrams to incorporate ligand topology as the input vectors. Utilizing persistence homology for machine learning in chemistry has been used by previous studies[76,77] and shown to be an effective descriptor for regression. This study utilized Ripser[78] for the generation of persistence images (PIs) that include connected components, and 1- (holes) and 2-dimensional (voids) homological descriptors by generating 100 × 100 square persistence images with a standard deviation of the Gaussian kernel (spread) of 0.009, an upper boundary of the PIs of 2.5 Å, and a lower boundary of the PIs of −0.1 Å. The SOAP descriptor used the positions of the H, C, N, O, and F atoms present for each individual structure and constructed the descriptor with a local region cutoff value of 4 Å, 6 radial basis functions, a maximum degree of spherical harmonics as 4, and set the output as a dense array as opposed to a sparse matrix. The persistence images coupled with the SOAP (SOAP + PI) for each ligand were used as the input vector with their respective $\log\beta$ values as y for random forest regression as implemented in the Scikit-learn package[79] using Python 3.10. The ML model utilized a 5-fold cross validation process with 200 trees, the mean absolute error loss function criteria, and six minimum samples per leaf for the analysis. The root mean square error was also calculated for each fold with the standard deviation of the error. We also investigated the performance of the individual descriptors on the datasets for comparisons with the coupled descriptors (see ESI Section S6†).

Data availability

The data for the following information are included in the ESI:† the dihedral rotation study, the potential energy surfaces, the top 50 functional groups from DFT optimization in terms of the highest $\log\beta$ values, the distribution of BTBP analogs in the different datasets used in this study, molecular representations of the validation set and the **CyMe$_4$–BTPhen**-based ligands used for active learning and transfer learning respectively, the active learning molecules, predicted and DFT $\log\beta$ values, and a narrative on the manual correction of some of the generated structures from molSimplify. Cartesian coordinates of all molecular structures and Jupyter Notebook are publicly available at **https://zenodo.org/records/14486728**, **https://10.5281/zenodo.15018297**. The code developed for the project that is presented in the submitted paper with the title "Ligand Design for ^{227}Ac Extraction by Active Learning and Molecular Topology" by Laub and Vogiatzis is deposited on GitHub (**https://github.com/Jeffrey-107/Code-for-Ligand-Design-for-Ac-227-Extraction-by-Active-Learning-and-Molecular-Topology**).

Author contributions

Jeffrey A. Laub: conceptualization, methodology, data generation, curation and visualization, formal analysis, workflow and ML model development, writing – original draft and editing. Konstantinos D. Vogiatzis: conceptualization, methodology, funding acquisition, project administration, writing – review and editing.

Conflicts of interest

The authors declare no competing financial interest.

Acknowledgements

This material is partially based upon work supported by the National Science Foundation under grant no. 2143354 (CAREER: CAS-Climate). The authors acknowledge the Infrastructure for Scientific Applications and Advanced Computing (ISAAC) of the University of Tennessee for computational resources.

References

1 R. M. Pallares and R. J. Abergel, *Front. Med.*, 2022, **9**, 1020188.
2 R. M. Pallares, M. Flick, K. M. Shield, T. A. Bailey, N. Velappan, A. M. Lillo and R. J. Abergel, *New J. Chem.*, 2022, **46**, 15795–15798.
3 T. Mastren, V. Radchenko, A. Owens, R. Copping, R. Boll, J. R. Griswold, S. Mirzadeh, L. E. Wyant, M. Brugh, J. W. Engle, F. M. Nortier, E. R. Birnbaum, K. D. John and M. E. Fassbender, *Sci. Rep.*, 2017, **7**, 8216.
4 S. Hogle, R. A. Boll, K. Murphy, D. Denton, A. Owens, T. J. Haverlock, M. Garland and S. Mirzadeh, *Appl. Radiat. Isot.*, 2016, **114**, 19–27.

 © 2025 The Author(s). Published by the Royal Society of Chemistry

Open Access Article. Published on 14 March 2025. Downloaded on 1/8/2026 1:14:21 AM. This article is licensed under a Creative Commons Attribution-NonCommercial 3.0 Unported Licence.

5 D. N. Shishkin, S. V. Krupitskii and S. A. Kuznetsov, *Radiochemistry*, 2011, **53**, 404–406.
6 R. A. Boll, D. Malkemus and S. Mirzadeh, *Appl. Radiat. Isot.*, 2005, **62**, 667–679.
7 D. S. Abou, J. Pickett, J. E. Mattson and D. L. J. Thorek, *Appl. Radiat. Isot.*, 2017, **119**, 36–42.
8 L. Qiu, J. Wu, N. Luo, Q. Xiao, J. Geng, L. Xia, F. Li, J. Liao, Y. Yang, J. Zhang and N. Liu, *Ind. Eng. Chem. Res.*, 2023, **62**, 14001–14011.
9 R. Perron, D. Gendron and P. W. Causey, *Appl. Radiat. Isot.*, 2020, **164**, 109262.
10 A. A. Kotovskii, N. A. Nerozin, I. V. Prokof'ev, V. V. Shapovaloc, A. Yu, A. S. Bolonkin and A. V. Dunin, *Radiochemistry*, 2015, **57**, 285–291.
11 L. Laughhunn, C. Botkin, W. Hubble, D. Hewing, J. Turner, R. Muzaffar, E. Robertson and M. Osman, *J. Nucl. Med.*, 2014, **55**, 2707.
12 V. Radchenko, A. Morgenstern, A. R. Jalilian, C. F. Ramogida, C. Cutler, C. Duchemin, C. Hoehr, F. Haddad, F. Bruchertseifer, H. Gausemel, H. Yang, J. A. Osso, K. Washiyama, K. Czerwinski, K. Leufgen, M. Pruszyński, O. Valzdorf, P. Causey, P. Schaffer, R. Perron, S. Maxim, D. S. Wilbur, T. Stora and Y. Li, *J. Nucl. Med.*, 2021, **62**, 1495–1503.
13 H. W. Kirby and L. R. Mordd, in *The Chemistry of the Actinide and Transactinide Elements*, Springer, 3rd edn, 2006, ch. 2, vol. 1, pp. 18–51.
14 R. H. Larsen, G. Henriksen and Ø. S. Brulard, *US Pat.*, US6635234B1, 2003.
15 BWXT, *Fusion Pharmaceuticals and BWXT Medical Announce Actinium-225 Partnership to Scale Supply for Developing Targeted Alpha Therapies*, accessed January 7, 2024.
16 BWXT, *BWXT Medical Expands Collaboration with Fusion Pharmaceuticals Through Strengthened Actinium Supply and Access to Generator Technology*, accessed January 7, 2024.
17 W. Yan, *ACS Cent. Sci.*, 2020, **6**, 827–829.
18 D. R. McAlister and E. P. Horwitz, *Appl. Radiat. Isot.*, 2018, **140**, 18–23.
19 P. J. Panak and A. Geist, *Chem. Rev.*, 2013, **113**, 1199–1236.
20 A. Bremer, D. M. Wittaker, C. A. Sharrad, A. Geist and P. J. Panak, *Dalton Trans.*, 2014, **43**, 2684–2694.
21 A. Bremer, C. M. Ruff, D. Girnt, U. Müllich, J. Rothe, P. W. Roesky, P. J. Panak, A. Karpov, T. J. J. Müller, M. A. Denecke and A. Geist, *Inorg. Chem.*, 2012, **51**, 5199–5207.
22 A. Afsar, P. Distler, L. M. Harwood, J. John and J. Westwood, *J. Org. Chem.*, 2016, **81**, 10517–10520.
23 C. Ekberg, E. Löfström-Engdahl, E. Aneheim, M. R. S. Foreman, A. Geist, D. Lundberg, M. Denecke and I. Persson, *Dalton Trans.*, 2015, **44**, 18395–18402.
24 M. R. S. Foreman, M. J. Hudson, M. G. B. Drew, C. Hill and C. Madic, *Dalton Trans.*, 2006, 1645–1653.
25 M. Steppert, I. Císařová, T. Fanghänel, A. Geist, P. Lindqvist-Reis, P. Panak, P. Štěpnička, S. Trumm and C. Walther, *Inorg. Chem.*, 2012, **51**, 591–600.
26 M. Nilsson, S. Andersson, F. Drouet, C. Ekberg, M. R. S. Foreman, M. Hudson, J.-O. Liljenzin, D. Magnusson and G. Skarnemark, *Solvent Extr. Ion Exch.*, 2006, **24**, 299–318.
27 P. Distler, M. Mindova, J. Sebesta, B. Gruner, D. Bavol, R. J. M. Egberink, W. Verboom, V. A. Babain and J. John, *ACS Omega*, 2021, **6**, 26416–26427.
28 A. Geist, C. Hill, G. Modolo, M. R. S. J. Foreman, M. Weigl, K. Gompper and M. J. Hudson, *Solvent Extr. Ion Exch.*, 2006, **24**, 463–483.
29 T. Vu, PhD thesis, Université Louis Pasteur (Strasbourg-I), 2008.
30 S. Trumm, P. J. Panak, A. Geist and T. Fanghänel, *Eur. J. Inorg. Chem.*, 2010, **2010**, 3022–3028.
31 G. J.-P. Deblonde, A. Ricano and R. J. Abergel, *Nat. Commun.*, 2019, **10**, 2438.
32 G. Modolo, A. Wilden, H. Daniels, A. Geist, D. Magnusson and R. Malmbeck, *Radiochim. Acta*, 2013, **101**, 155–162.
33 N. Kemnitz, D. E. Hammond, P. Henderson, E. Le Roy, M. Charette, W. Moore, R. F. Anderson, M. Q. Fleisher, A. Leal, E. Black, C. T. Hayes, J. Adkins, W. Berelson and X. Bian, *Mar. Chem.*, 2023, **250**, 104180.
34 G. Choppin, J.-O. Liljenzin, J. Rydberg and C. Ekberg, *Radiochemistry and Nuclear Chemistry*, Academic Press, Oxford, U.K., 4th edn, 2013.
35 S. M. Lyons, C. G. Britt, L. S. Wood, D. L. Duke, B. G. Fulsom, M. E. Moore and L. Snyder, *AIP Adv.*, 2023, **13**, 085115.
36 C. Qin, J. Liu, Y. Yu, Z. Xu, J. Du, G. Jiang and L. Zhao, *Ceram. Int.*, 2024, **50**, 1220–1230.
37 E. Stippell, L. Alzate-Vargas, K. N. Subedi, R. M. Tutchton, M. W. D. Cooper, S. Tretiak, T. Gibson and R. A. Messerly, *Artificial Intelligence Chemistry*, 2024, **2**, 100042.
38 J. Wang, D. B. Ghosh and Z. Zhang, *Materials*, 2023, **16**, 4985.
39 A. Ghosh, F. Ronning, S. M. Nakhmanson and J.-X. Zhu, *Phys. Rev. Mater.*, 2020, 064414.
40 E. T. Dubois, J. Tranchida, J. Bouchet and J.-B. Maillet, *Phys. Rev. Mater.*, 2024, **8**, 025402.
41 K. Zheng, N. Marcella, A. L. Smith and A. I. Frenkel, *J. Phys. Chem. C*, 2024, **128**, 7635–7642.
42 M.-T. Nguyen, R. Rousseau, P. D. Paviet and V.-A. Glezakou, *ACS Appl. Mater. Interfaces*, 2021, **13**, 53398–53408.
43 T. Liu, K. R. Johnson, S. Jansone-Popova and D.-e. Jiang, *JACS Au*, 2022, **2**, 1428–1434.
44 M.-T. Nguyen, B. A. Helfrecht, R. Rousseau and V.-A. Glezakou, *J. Mol. Liq.*, 2022, **365**, 120115.
45 D. A. Penchoff, C. C. Peterson, E. M. Wrancher, G. Bosilca, R. J. Harrison, E. F. Valeev and P. D. Benny, *J. Radioanal. Nucl. Chem.*, 2022, **331**, 5469–5485.
46 T. Chen and C. Guestrin, *XGBoost: A Scalabale Tree Boosting System*, 2016, preprint, arXiv:1603.02754, DOI: 10.1145/2939672.2939785.
47 D. Rogers and M. Hahn, *J. Chem. Inf. Model.*, 2010, **50**, 742–754.
48 G. Landrum, *RDKit: Open-Source Cheminformatics*, https://www.rdkit.org.
49 D. Lundberg and I. Persson, *Coord. Chem. Rev.*, 2016, **318**, 131–134.
50 J. A. Laub and K. D. Vogiatzis, *J. Phys. Chem. A*, 2023, **127**, 5523–5533.

Open Access Article. Published on 14 March 2025. Downloaded on 1/8/2026 1:14:21 AM.
This article is licensed under a Creative Commons Attribution-NonCommercial 3.0 Unported Licence.

51 V. Hubscher-Bruder, J. Haddaoui, S. Bouhroum and F. Arnaud-Neu, *Inorg. Chem.*, 2010, **49**, 1363–1371.
52 F. W. Lewis, L. M. Harwood, M. J. Hudson, M. G. B. Drew, V. Hubscher-Bruder, V. Videva, F. Arnaud-Neu, K. Stamberg and S. Vyas, *Inorg. Chem.*, 2013, **52**, 4993–5005.
53 E. I. Ioannidis, T. Z. Gani and H. J. Kulik, *J. Comput. Chem.*, 2016, **37**, 2106–2117.
54 N. M. O'Boyle, C. Morley and G. R. Hutchison, *Chem. Cent. J.*, 2008, **2**, 5.
55 N. M. O'Boyle, M. Banck, C. A. James, C. Morley, T. Vandermeersch and G. R. Hutchison, *J. Cheminf.*, 2011, **3**, 33.
56 T. Fink, H. Bruggesser and J.-L. Reymond, *Angew. Chem., Int. Ed.*, 2005, **44**, 1504–1508.
57 T. Fink and J.-L. Reymond, *J. Chem. Inf. Model.*, 2007, **47**, 342–353.
58 F. Neese, *Wiley Interdiscip. Rev.: Comput. Mol. Sci.*, 2012, **2**, 73–78.
59 F. Neese, F. Wennmohs, U. Becker and C. Riplinger, *J. Chem. Phys.*, 2020, **152**, 224108.
60 F. Neese, *Wiley Interdiscip. Rev.: Comput. Mol. Sci.*, 2022, **12**, 1606.
61 K. Lyczko and S. Ostrowski, *Nukleonika*, 2015, **60**, 853–857.
62 E. van Lenthe, J. G. Snijders and E. J. Baerends, *J. Chem. Phys.*, 1996, **105**, 6505–6516.
63 D. A. Pantazis and F. Neese, *J. Chem. Theory Comput.*, 2011, **7**, 677–684.
64 V. Barone and M. Cossi, *J. Phys. Chem. A*, 1998, **102**, 1995–2001.
65 P. Panda and S. Mishra, *Chem. Phys. Impact*, 2024, **8**, 100447.
66 J. P. Perdew, *Phys. Rev. B: Condens. Matter Mater. Phys.*, 1986, **33**, 8822–8824.
67 A. D. Becke, *Phys. Rev. A: At., Mol., Opt. Phys.*, 1988, **38**, 3098–3100.
68 F. Weigend and R. Ahlrichs, *Phys. Chem. Chem. Phys.*, 2005, **7**, 3297–3305.
69 D. A. Pantazis, X.-Y. Chen, C. R. Landis and F. Neese, *J. Chem. Theory Comput.*, 2008, **4**, 908–919.
70 G. A. McCarver, R. J. Hinde and K. D. Vogiatzis, *Inorg. Chem.*, 2020, **59**, 10492–10500.
71 A. N. Srivastva, *Stability and Application of Coordination Compounds*, IntechOpen, London, 2020.
72 H. Adams, T. Emerson, M. Kirby, R. Neville, C. Peterson, P. Shipman, S. Chepushtanova, E. Hanson, F. Motta and L. Ziegelmeier, *J. Mach. Learn. Res.*, 2017, **18**, 1–35.
73 G. M. Jones, B. Story, V. Maroulas and K. D. Vogiatzis, *Molecular Representations for Machine Learning*, Am. Chem. Soc., 2023.
74 L. Himanen, M. O. J. Jäger, E. V. Morooka, F. F. Canova, Y. S. Ranawat, D. Z. Gao, P. Rinke and A. S. Foster, *Comput. Phys. Commun.*, 2020, **247**, 106949.
75 J. Laakso, L. Himanen, H. Homm, E. V. Morooka, M. O. J. Jäger, M. Todorović and P. Rinke, *J. Chem. Phys.*, 2023, **158**, 234802.
76 G. M. Jones, B. A. Smith, J. K. Kirkland and K. D. Vogiatzis, *Inorg. Chem. Front.*, 2023, **10**, 1062–1075.
77 J. Townsend, C. P. Micucci, J. H. Hymel, V. Maroulas and K. D. Vogiatzis, *Nat. Commun.*, 2020, **11**, 3230.
78 U. Bauer, *J. Appl. Comput. Topol.*, 2021, **5**, 391–423.
79 F. Pedregosa, G. Varoquaux, A. Gramfort, V. Michel, B. Thirion, O. Grisel, M. Blondel, P. Prettenhofer, R. Weiss, V. Dubourg, J. Vanderplas, A. Passos, D. Cournapeau, M. Brucher and M. P. É. Duchesnay, *J. Mach. Learn. Res.*, 2011, **12**, 2825–2830.

 © 2025 The Author(s). Published by the Royal Society of Chemistry